INTERNATIONAL JOURNAL FOR NUMERICAL METHODS IN FLUIDS
Int. J. Numer. Meth. Fluids 2010; **62**:473–498
Published online 27 October 2009 in Wiley InterScience (www.interscience.wiley.com). DOI: 10.1002/fld.2021

High-order shock capturing schemes for turbulence calculations

S.-C. Lo*,†, G. A. Blaisdell and A. S. Lyrintzis

School of Aeronautics and Astronautics, Purdue University, West Lafayette, IN 47907, U.S.A.

SUMMARY

This work investigates high-order central compact methods for simulating turbulent supersonic flows that include shock waves. Several different types of previously proposed characteristic filters, including total variation diminishing, monotone upstream-centered scheme for conservation laws, and weighted essentially non-oscillatory filters, are investigated in this study. Similar to the traditional shock capturing schemes, these filters can eliminate the numerical instability caused by large gradients in flow fields, but they also improve efficiency compared with classical shock-capturing schemes. Adding the nonlinear dissipation part of a classical shock-capturing scheme to a central scheme makes the method suitable for incorporation into any existing central-based high-order subsonic code. The amount of numerical dissipation to add is sensed by means of the artificial compression method switch. In order to improve the performance of the characteristic filters, we propose a hybrid approach to minimize the dissipation added by the characteristic filter. Through several numerical experiments (including a shock/density wave interaction, a shock/vortex interaction, and a shock/mixing layer interaction) we show that our hybrid approach works better than the original method, and can be used for future turbulent flow simulations that include shocks. Copyright © 2009 John Wiley & Sons, Ltd.

Received 18 June 2008; Revised 20 January 2009; Accepted 21 January 2009

KEY WORDS: high-order finite-difference method; compact scheme; filter; spatial filter; characteristic filter; shock capture; supersonic turbulent flow

1. INTRODUCTION

Numerical simulation of high speed turbulent flows can be applied in many fields, such as helicopter/propeller/fan blade tips operating at supersonic speeds, mixing enhancement in a supersonic combustion ramjet engine, and supersonic jet noise, which is the application we are

*Correspondence to: S.-C. Lo, School of Aeronautics and Astronautics, Purdue University, West Lafayette, IN 47907, U.S.A.
†E-mail: sclo@purdue.edu

Contract/grant sponsor: Purdue Research Foundation (PRF)/Computing Research Institute (CRI) Special Incentive Research Grant (SIRG)

interested in. The common features of these flow fields are vortices and shocks. A high-order central scheme is required to preserve the vortical flow structures; however, it does not have shock capturing ability. At the same time, traditional shock capturing schemes are usually too dissipative and not suitable for turbulence simulations. In order to capture the shocks while preserving the vortical flow structures, this study investigates numerical methods for extending subsonic turbulence calculations, based on large eddy simulations (LES) or direct numerical simulation (DNS), to supersonic flows that include shocks. This serves as an approach toward supersonic jet simulations.

Jet noise is the main source of noise during aircraft takeoff. Owing to the strict regulations regarding noise emission, the cost of operating current commercial aircraft has increased and the expansion of air travel has been stifled. Even when airplanes are cruising far from populated areas, jet engine noise is still a serious issue for passenger comfort. Noise issues become more severe for supersonic aircraft and some subsonic commercial jets (such as the Boeing 777 and 787) with high bypass ratio engines. In addition to the turbulent mixing noise, when a supersonic jet engine operates at an off-design condition shock cell noise can be generated. In order to help us gain a better understanding of supersonic jet noise and develop a reliable prediction tool, we follow a high-order computational fluid dynamics approach that provides an efficient way to achieve these goals.

High-order central numerical methods are typically used in DNSs and LES of turbulent flows as well as in computational aeroacoustics. This is because high-order schemes can resolve a wider range of length scales than traditional second-order accurate methods and they reduce dissipative numerical errors. However, they are often perceived as less robust and hard to code due to the large stencil size required. The compact method proposed by Lele [1] can remedy this problem. For the same order of accuracy, by solving for the flux derivative implicitly, a smaller stencil size is required than for explicit central-difference schemes and, therefore, the boundary condition treatment is simplified. In addition, the compact schemes contain a smaller truncation error compared with non-compact schemes of equal order. However, in order to eliminate high-frequency errors that give rise to numerical instabilities while retaining high-order accuracy, filtering of the computed solutions is required. Either explicit or implicit spatial filters can perform this task. The role of a spatial filter is similar to that of the more popular artificial dissipation method, but the derivation of the former approach is relatively less dependent on the governing equations being solved [2, 3]. The compact scheme combined with spatial filters has been used successfully in three-dimensional LES for turbulent jet noise prediction by several investigators [4–6].

When the flow field includes shocks or large gradients, the application of a compact scheme and a spatial filter in these regions results in spurious oscillations and causes numerical instabilities. Therefore, unlike the artificial dissipation method, the spatial filter is inadequate for predicting high speed flows that involve shocks. One approach is to modify the compact scheme, as done by Xie *et al.* [7]. Another approach is to use filters. Yee *et al.* [8] proposed another class of filters, called characteristic filters, which add the dissipative part of traditional shock capture schemes to nondissipative central-based schemes to damp out numerical instabilities caused by shocks. Owing to this feature, characteristic filters are very suitable to incorporate into existing LES codes based on high-order central methods, and they enhance the codes to have shock capturing capability. In addition, since these filters can be applied to solutions once after each full time step, their computational cost is considerably less than that of traditional shock capturing schemes such as total variation diminishing (TVD), monotone upstream-centered scheme for conservation laws (MUSCL), and (weighted) essentially non-oscillatory (ENO/WENO) schemes.

DOI: 10.1002/fld

It has been shown that in turbulent flows or in aeroacoustics the application of these traditional shock capturing schemes in the entire domain is not very suitable, because they can lead to significant damping of the turbulent or acoustic fluctuations [9, 10]. Our numerical experiments show that the same phenomenon happens for the application of characteristic filters. In order to remedy this problem and to achieve minimal dissipation, we propose a hybrid approach which combines the compact scheme, spatial filter, and characteristic filter. In other words, by using a shock detecting function, the characteristic filter can be applied only in the large gradient regions (i.e. shocks) and the implicit spatial filter is applied to other smooth regions instead. This approach is similar to the hybrid compact-Roe scheme of Visbal and Gaitonde [11].

In this work, we examine several different types of characteristic filters, including the TVD and MUSCL types proposed by Yee *et al*. [8], and the ENO/WENO-type proposed by Garnier *et al*. [12]. The formulations of the governing equations, various types of filters, and shock detectors are presented in Section 2. In Section 3, we evaluate the performance of different characteristic filters through several test cases. We also compare the results of applying the characteristic filters in the whole computational domain and in the shock regions only. Finally, the conclusions are summarized in Section 4. An earlier version of this work can be found in Reference [13].

2. NUMERICAL METHODS

2.1. Governing equations

The governing equations are the nondimensional compressible Navier–Stokes equations written in conservation form. In two-dimensional space the governing equations written in Cartesian coordinates have the following form:

$$\frac{\partial U}{\partial t}+\frac{\partial E}{\partial x}+\frac{\partial F}{\partial y}=\frac{\partial E_v}{\partial x}+\frac{\partial F_v}{\partial y}$$

The conservative vector U, convective fluxes E and F, and viscous fluxes E_v and F_v are given by

$$U=\begin{bmatrix}\rho\\ \rho u\\ \rho v\\ e\end{bmatrix},\quad E=\begin{bmatrix}\rho u\\ \rho u^2+P\\ \rho uv\\ (e+P)u\end{bmatrix},\quad F=\begin{bmatrix}\rho v\\ \rho uv\\ \rho v^2+P\\ (e+P)v\end{bmatrix} \tag{1}$$

$$E_v=\begin{bmatrix}0\\ \tau_{xx}\\ \tau_{xy}\\ u\tau_{xx}+v\tau_{xy}+q_x\end{bmatrix},\quad F_v=\begin{bmatrix}0\\ \tau_{xy}\\ \tau_{yy}\\ u\tau_{xy}+v\tau_{yy}+q_y\end{bmatrix} \tag{2}$$

where t is nondimensional time, ρ is the density, u and v are the x and y velocity components, respectively, e is the total energy, and P is the pressure. τ_{ij} and q_i are the viscous stress tensor and conductive heat flux, respectively.

DOI: 10.1002/fld

2.2. Time advancement scheme

Two time advancement schemes are used in the current study. The first one is the third-order accurate TVD Runge–Kutta method proposed by Shu and Osher [14]

$$U^{(1)} = U^n + \Delta t\, L(U^n) \tag{3}$$

$$U^{(2)} = \tfrac{3}{4}U^n + \tfrac{1}{4}U^{(1)} + \tfrac{1}{4}\Delta t\, L(U^{(1)}) \tag{4}$$

$$\hat{U}^{n+1} = \tfrac{1}{3}U^n + \tfrac{2}{3}U^{(2)} + \tfrac{2}{3}\Delta t\, L(U^{(2)}) \tag{5}$$

The second one is the classical fourth-order Runge–Kutta method which has the form

$$k_1 = L(U^n) \tag{6}$$

$$k_2 = L\left(U^n + \frac{\Delta t}{2}k_1\right) \tag{7}$$

$$k_3 = L\left(U^n + \frac{\Delta t}{2}k_2\right) \tag{8}$$

$$k_4 = L(U^n + \Delta t k_3) \tag{9}$$

$$\hat{U}^{n+1} = U^n + \frac{\Delta t}{6}[k_1 + 2k_2 + 2k_3 + k_4] \tag{10}$$

where L represents the right-hand side of the Navier–Stokes equations evaluated using a base spatial differencing scheme which can be any high-order non-dissipative method, such as that described in the following section, and Δt is the time step.

2.3. Base spatial discretization scheme

To compute spatial derivatives, the sixth-order non-dissipative compact finite difference scheme developed by Lele [1] is used for the current study. The method is formulated as follows:

$$\frac{1}{3}f'_{i-1} + f'_i + \frac{1}{3}f'_{i+1} = \frac{7}{9\Delta x}(f_{i+1} + f_{i-1}) + \frac{1}{36\Delta x}(f_{i+2} + f_{i-2}) \tag{11}$$

where f' is the derivative of the function f. Computation of the derivative f' requires solution of a tri-diagonal linear system of equations. However, the implicit nature of the scheme allows for a smaller stencil size (hence, the name compact scheme), which makes implementation near boundaries easier. In addition, this method has better spatial wave number resolution than explicit methods of the same order of accuracy. When a nonuniform grid is used, such as in the mixing layer test problem, the nonuniform grid in physical space is mapped onto a uniformly spaced computational grid and the difference formula is applied on the uniform grid.

2.4. Low-pass spatial filter

The compact scheme is a high-order accurate, non-dissipative, centered scheme. However, like other centered schemes, it produces high-frequency spurious modes that originate from nonperiodic boundary conditions, stretched grids, or nonlinear interactions, and cause numerical instabilities. In order to eliminate these spurious modes and keep the scheme stable, filtering of the computed

DOI: 10.1002/fld

solution is employed. The tenth-order tri-diagonal spatial filter proposed by Gaitonde and Visbal [15] is used for the current study. This compact-type filter is applied to the conservative variables once per time step. Denoting the pre-filtered value by $\hat{U}$ (which is the solution after a full Runge–Kutta time step described in the above section), the filtered value, $\bar{U}$, is obtained by solving the system

$$\alpha_f \bar{U}_{i-1} + \bar{U}_i + \alpha_f \bar{U}_{i+1} = \sum_{n=0}^{N} \frac{a_n}{2} (\hat{U}_{i+n} + \hat{U}_{i-n}) \tag{12}$$

where a_n are filter coefficients and $N=5$ for tenth-order accuracy. α_f is a filter parameter that controls how much of the high wave number range is filtered. In this study, α_f is set to 0.48. As the filter is applied only once per time step, its cost is not as significant as that of the compact spatial derivative when time advancing the governing equations.

2.5. *Characteristic (ACM) filter*

Even though compact spatial filters can suppress numerical instabilities due to high-frequency modes, they fail around large gradients and discontinuities. Yee *et al.* [8] proposed characteristic-based filters which can maintain the non-dissipative nature of high-order spatial differencing schemes away from shocks, while being capable of capturing shocks. The basic idea is to add the filter numerical flux which is computed from the nonlinear dissipation of a TVD, MUSCL, or ENO/WENO scheme to the non-dissipative high-order central scheme. The filter operator, L_f, is

$$L_f(F^*, G^*)_{i,j} = \frac{1}{\Delta x}(\tilde{F}^*_{i+1/2,j} - \tilde{F}^*_{i-1/2,j}) + \frac{1}{\Delta y}(\tilde{G}^*_{i,j+1/2} - \tilde{G}^*_{i,j-1/2}) \tag{13}$$

where $\tilde{F}^*$ and $\tilde{G}^*$ are the x and y direction filter numerical fluxes evaluated using $\hat{U}^{n+1}$ (which is the solution after a full Runge–Kutta step described in Section 2.3). Then, the filtered value, $U_{i,j}$, at the new time level $n+1$ becomes

$$U^{n+1}_{i,j} = \hat{U}^{n+1}_{i,j} - \Delta t\, L_f(F^*, G^*)_{i,j} \tag{14}$$

This filtering process can be applied either at the end of a full time step or after each sub-stage of a Runge–Kutta integration. For computational efficiency, in our current study we use the former approach.

The Harten switch [16] (originally designed for the self-adjusting hybrid schemes) can switch from a higher-order scheme to Harten's first-order artificial compression method (ACM) scheme for shock capturing. Instead of switching to a first-order scheme, following the idea of the ACM method, a low-dissipative high-order shock-capturing scheme can be achieved by using a nonlinear characteristic filter [8]. The nonlinear dissipation is multiplied by the Harten switch. This switch signals the amount of nonlinear dissipation to be added to the base scheme. The general formulas of the filter numerical flux from Yee *et al.* [8] are summarized as follows:

$$\tilde{F}^{*\mathrm{TVD/MUSCL}}_{i+1/2,j} = \tfrac{1}{2} R_{i+1/2} \Phi^*_{i+1/2} \tag{15}$$

$$\phi^{l*}_{i+1/2} = \kappa \theta^l_{i+1/2} \phi^l_{i+1/2} \tag{16}$$

where $R_{i+1/2}$ is the right eigenvector matrix of the flux Jacobian $\partial F/\partial U$ evaluated by Roe's approximate average state [17]. F and U are the x direction convective flux and the conservative

DOI: 10.1002/fld

vector as defined in the previous section; $\phi^{l*}_{i+1/2}$ are the elements of $\Phi^*_{i+1/2}$ with $\phi^l_{i+1/2}$ evaluated by a TVD or MUSCL scheme; κ is a problem-dependent parameter with a range $0.03 \leqslant \kappa \leqslant 2$. Our numerical experiments show that TVD and MUSCL filters are more sensitive to the choice of κ than the WENO filter. In order to make a comparison between filters, κ is fixed at 1 for all the cases in this paper. For the choice of optimized values of κ in different cases, the reader should refer to the original Reference [8] for more details. $\theta^l_{i+1/2}$ is the Harten switch that has the form

$$\theta^l_{i+1/2} = \max(\widehat{\theta}^l_{i-m+1}, \ldots, \widehat{\theta}^l_{i+m}) \tag{17}$$

where

$$\hat{\theta}^l_i = \left| \frac{|\alpha^l_{i+1/2}| - |\alpha^l_{i-1/2}|}{|\alpha^l_{i+1/2}| + |\alpha^l_{i-1/2}|} \right|^p \tag{18}$$

$\alpha^l_{i+1/2}$ are the elements of $R^{-1}_{i+1/2}(U_{i+1} - U_i)$ for TVD and $R^{-1}_{i+1/2}(U^R_{i+1/2} - U^L_{i+1/2})$ for MUSCL. Yee *et al.* [8] modify this switch to $\theta^l_{i+1/2} = \max(\hat{\theta}^l_i, \hat{\theta}^l_{i+1})$ and set p equal to 1, and we follow Yee's formulas in the current study.

Three variations of the TVD scheme [18]—the Harten–Yee upwind (HYTVD), the Yee–Roe–Davis symmetric (YRDTVD), and the Roe–Sweby upwind (RSTVD)—are compared in the following section. For brevity, the detailed TVD formulas are not shown here and can be found in the original references. The limiters used with the TVD methods are $\min\mathrm{mod}(\alpha^l_{i-1/2}, \alpha^l_{i+1/2})$ for the HYTVD, $\min\mathrm{mod}(2\alpha^l_{i-1/2}, 2\alpha^l_{i+1/2}, 2\alpha^l_{i+3/2}, (\alpha^l_{i-1/2} + \alpha^l_{i+3/2})/2)$ for the YRDTVD, and $\min\mathrm{mod}(1, r)$ for the RSTVD, where the formula for r can be found in the same reference. In [19] it is pointed out that less dissipative results can be obtained with the HYTVD scheme by using a different limiter; however, only the limiters given above are used in the current study.

The MUSCL-type scheme [18] is summarized as follows:

$$\phi^l_{i+1/2} = \psi(a^l_{i+1/2})\alpha^l_{i+1/2} \tag{19}$$

$$\alpha^l_{i+1/2} = R^{-1}_{i+1/2}(U^R_{i+1/2} - U^L_{i+1/2}) \tag{20}$$

where ψ is the Harten entropy correction function, and $a^l_{i+1/2}$ and $R_{i+1/2}$ are the eigenvalues and eigenvectors of the flux Jacobian $\partial F/\partial U$ evaluated using a symmetric average of $U^R_{i+1/2}$ and $U^L_{i+1/2}$ (i.e. Roe average). In here, $U^R_{i+1/2}$ and $U^L_{i+1/2}$ are evaluated by an upwind-biased interpolation from neighboring grid points with the minmod limiter imposed and the compression factor within the minmod limiter equal to 4.

Garnier *et al.* [12] proposed a characteristic filter using the ENO/WENO scheme. The dissipative numerical flux is written as

$$\tilde{F}^{*\mathrm{ENO/WENO}}_{i+1/2,j} = R_{i+1/2}\Phi^*_{i+1/2} \tag{21}$$

$$\phi^{l*}_{i+1/2} = \kappa\theta^l_{i+1/2}\phi^l_{i+1/2} \tag{22}$$

Here, $\phi^l_{i+1/2}$ is obtained by subtracting an mth-order centered scheme (F_C) from an rth-order ENO/WENO scheme (F), as follows:

$$\phi^l_{i+1/2} = F - F_C \tag{23}$$

DOI: 10.1002/fld

where F and F_C are numerical fluxes, which are interpolated from nearby grid points by the ENO/WENO approach. Either the Roe-type or the flux splitting-type ENO/WENO scheme can be chosen. Our current study implements the latter one with the local Lax–Friedrichs splitting technique. This ENO/WENO filter with a fourth-order central-based scheme has been used in a LES simulation of 3-D shock/boundary-layer interaction [20], and the results show a very good agreement with the experimental data. There are other similar WENO filters in Reference [21, 22] and a detailed formulation of the ENO/WENO scheme can be found in Reference [23].

2.6. *Shock detectors*

As reported by Lee *et al.* [10] the use of a 6th-order accurate ENO scheme for the entire domain adds too much dissipation such that turbulent fluctuations are excessively damped. Our numerical experiments show that a similar situation happens for the low-order filter (e.g. TVD filter) when using it in the entire domain. Another problem is that when the high-order compact spatial filters are used with shocks or large gradients, spurious oscillations occur resulting in a numerical instability; therefore, they cannot be used in the entire domain either. In order to address these problems, a shock detector can be used as a sensor to switch between the spatial filters and the ACM filters. Defining the shock detector function, Ω_i, and a threshold parameter, σ, the ACM filter is then applied locally in the region where a threshold criterion is exceeded, given by $\Omega_i > \sigma$. A single value of $\sigma = 0.01$ is used in our work, and the effects of the choice of σ are investigated in the following section.

After identifying the shock region, the switch between the ACM filter and the spatial filter near the shock region is illustrated in the schematic of Figure 1. Within the shock region, including shock points and two buffer points on each side, we apply only the ACM filter and disable the spatial filter. This is done by setting the filter parameter, α_f, to 0.5 in the shock region. Outside the shock zone, the order of the spatial filter gradually increases from second order ($F2$) to tenth order ($F10$). Because of the buffer points, the stencil of the spatial filter does not include the shock points.

For multi-dimensional turbulent simulations, Ducros *et al.* [24] proposed a shock detector which is capable of distinguishing turbulent fluctuations from large gradients and shocks. This is done

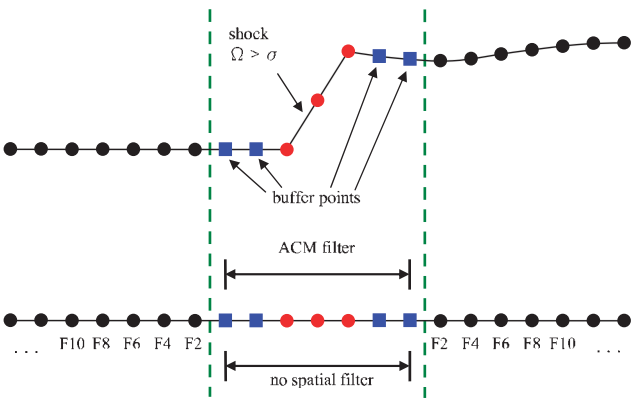

Figure 1. Schematic of hybrid compact scheme, ACM filter and the order of the spatial filter near the shock region.

DOI: 10.1002/fld

by multiplying the Jameson sensor [25] by another factor proposed by them, that is

$$\Omega_i = \left| \frac{P_{i+1} - 2P_i + P_{i-1}}{P_{i+1} + 2P_i + P_{i-1}} \right| \frac{(\mathrm{div}(\mathbf{u}))^2}{(\mathrm{div}(\mathbf{u}))^2 + (\mathrm{rot}(\mathbf{u}))^2} \tag{24}$$

where P and $\mathbf{u}$ are the pressure and velocity vector, respectively. Obviously, the second part of the sensor cannot be used in one-dimensional problems; therefore, it is only used in our two-dimensional test cases.

For the one-dimensional study, a WENO-type smoothness criterion [11] is used as a shock detector, which is given by

$$\Omega_i = [a(P_{i+1} - P_{i-1})^2 + b(P_{i+1} - 2P_i + P_{i-1})^2]^n \tag{25}$$

where a and b are defined in the fifth-order WENO scheme (i.e. $a = \frac{1}{4}$ and $b = \frac{13}{12}$), and n is set equal to 2 in order to sharpen the shock detection region. P is the pressure. Here the WENO smoothness criterion is used only for the shock detector and it is not related to the accuracy of the spatial discretization. A more sophisticated shock detection scheme is available in [26] (with source code available in [19]), although in the current study we only consider the two shock detectors listed above.

3. NUMERICAL EXPERIMENTS AND DISCUSSION OF RESULTS

3.1. Shock tube problem

The first case is a 1-D quite mild shock tube problem. This case is just used to illustrate the influence of shocks on the compact scheme and spatial filter. The computation covers a domain $x \in [0, 1]$ and the nondimensional initial condition is specified as

$$[\rho, u, P] = [1, 0, 3] \quad \text{for } x < 0.5 \tag{26}$$

$$[\rho, u, P] = [1, 0, 1] \quad \text{for } x \geqslant 0.5 \tag{27}$$

and it generates a Mach 1.35 moving shock. Since this shock is weak, the numerical oscillations generated by the compact scheme do not cause the solver to crash by the output time. The solution is integrated with a CFL number equal to 0.01 until $t = 0.15$. A uniform mesh with a total of 201 grid points is used in this case. The reference solution is computed by an exact Riemann solver.

We compare two different approaches: the compact scheme plus the spatial filter, and the compact scheme plus the characteristic filter, and show that the spatial filter is not applicable in the high gradient (or shock) regions. The characteristic filter we use in this case is the WENO filter. It is well known that computing with the compact scheme alone generates significant oscillations around the shock, contact discontinuity, expansion fan, and boundaries. Most of these oscillations can be damped out if we add the spatial filter as shown in Figure 2. However, we still can see some oscillations near the shock and contact discontinuity. If the shock strength increases, these oscillations will also increase and finally cause the solver to crash. Therefore, the spatial filter cannot be used in the shock region. If we replace the spatial filter with the characteristic filter then we can damp out all the oscillations, as shown in the same figure.

In order to understand the maximum allowable moving shock Mach number for each type of ACM filter, we perform several numerical experiments on this 1-D shock tube problem. This is done by increasing the left initial pressure in Equation (26) (hence, the initial pressure ratio and the

DOI: 10.1002/fld

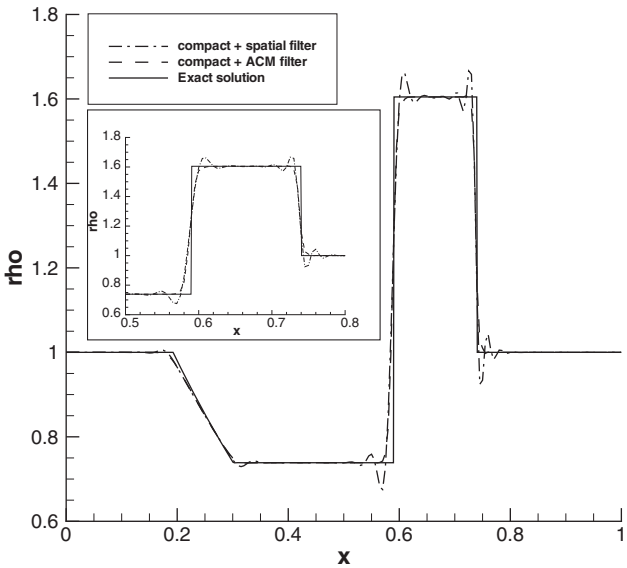

Figure 2. Comparison of spatial filter, and characteristic filter. (201 points uniform mesh.)

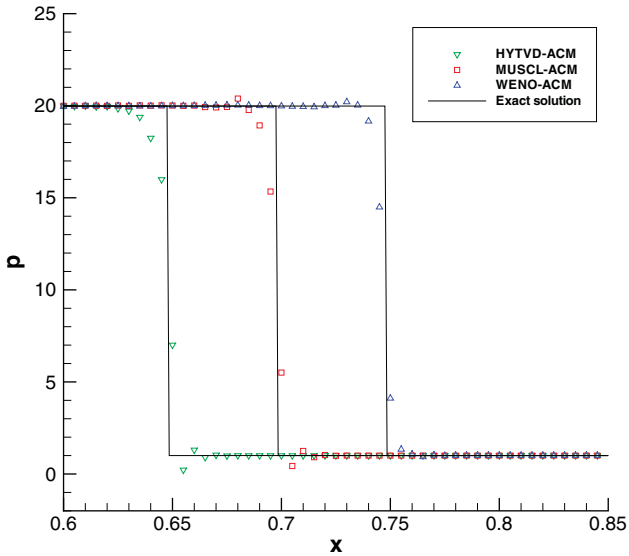

Figure 3. Comparison of a Mach 4.2 moving shock. (201 points uniform mesh. The x coordinate is shifted by 0.05 for each successive case for clarity.)

moving shock Mach number). Numerical experiments show that all three types of characteristic filters (HYTVD, MUSCL, and WENO) can resolve a Mach 4.2 moving shock without significant oscillation. Figure 3 shows the enlarged view of this Mach 4.2 moving shock computed by each

DOI: 10.1002/fld

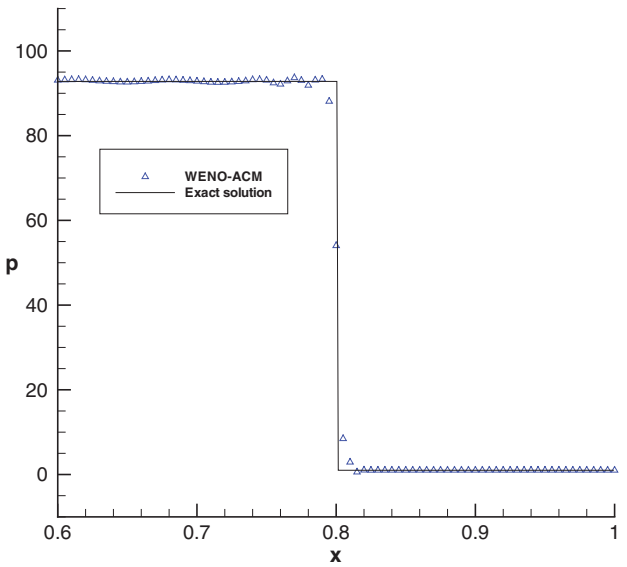

Figure 4. Mach 8.9 moving shock computed by the WENO filter. (201 points uniform mesh.)

filter at the same time. The exact solution (computed by an exact Riemann solver) is also given by a solid line for comparison with each numerical solution. The x axis is shifted by 0.05 for each case to increase readability. It is worth mentioning that the WENO filter can even resolve a Mach 8.9 moving shock, as shown in Figure 4. At this Mach number the maximum amplitude of the oscillations in pressure is still less than 1.0% of the pressure jump across the shock. Note, however, that the pressure in the driven section is low, and beyond this Mach number oscillations result in a negative value of pressure and failure of the solver. It should be noted that the goal of testing this case is not to show excellent agreement. Instead, we are testing the limits of the method.

3.2. Shock/density oscillation interaction

This test case is a 1-D inviscid moving shock/density wave interaction [14], which consists of the interaction of a moving Mach 3 shock with a density fluctuation. The nondimensional initial condition is specified as

$$[\rho, u, P] = [3.857143, 2.269369, 10.33333] \quad \text{for } x < -4 \tag{28}$$

$$[\rho, u, P] = [1 + 0.2\sin(5x), 0, 1] \quad \text{for } x \geqslant -4 \tag{29}$$

and the computation covers a domain $x \in [-5, 5]$. The solution is integrated with a CFL number equal to 0.3 until $t = 1.8$. A uniform mesh with a total of 401 grid points is used in this case. The reference solution, computed with a fifth-order accurate WENO scheme with 1601 grid points, and the initial conditions are shown in Figure 5. Results computed using three different (i.e. TVD, MUSCL, and WENO) filters are presented. In the first approach, we apply the ACM filter in the entire computational domain; therefore, no spatial filter is applied. These results are shown in Figures 6 and 7. In the second approach, shown in Figures 8 and 9, the ACM filter is only applied in the shock regions and the 10th-order spatial filter is used in the smooth regions. The

DOI: 10.1002/fld

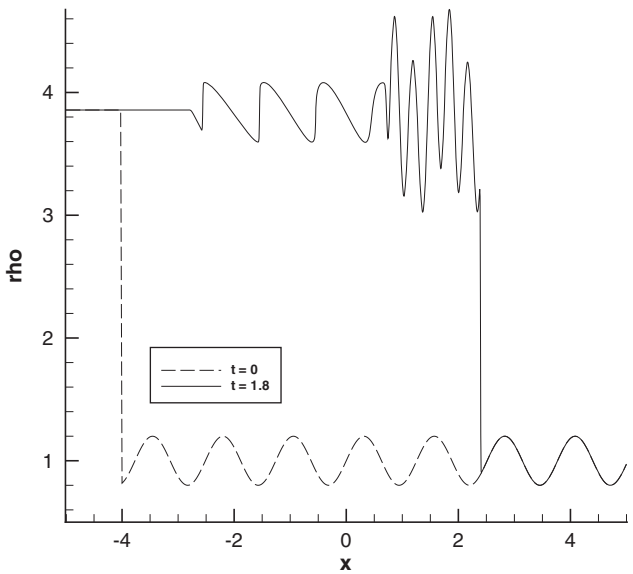

Figure 5. Initial density distribution and final reference solution.

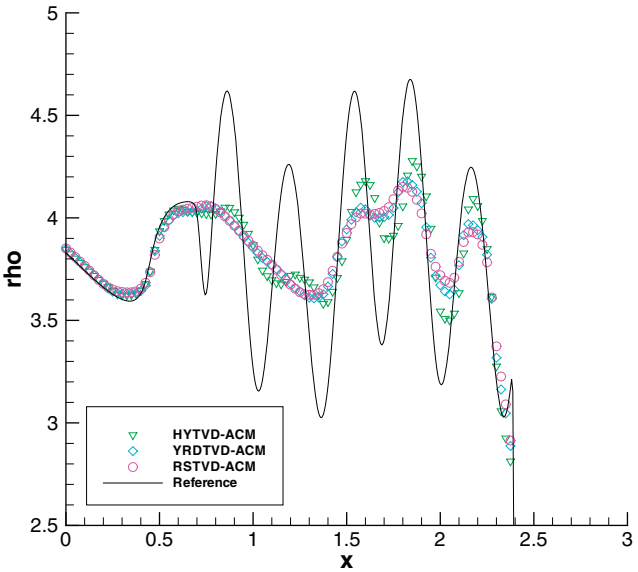

Figure 6. Density distribution at $t = 1.8$ with TVD filters applied globally.

WENO-type shock detector (Equation (25)) is used to detect the shock regions. The threshold parameter, σ, is set to 0.01, and the effect of this factor is examined later.

As the results show (using the same grid points) the high-order filters (MUSCL and WENO filters, Figures 7 and 9) are less dissipative than the low-order filters (TVD filters, Figures 6 and 8).

DOI: 10.1002/fld

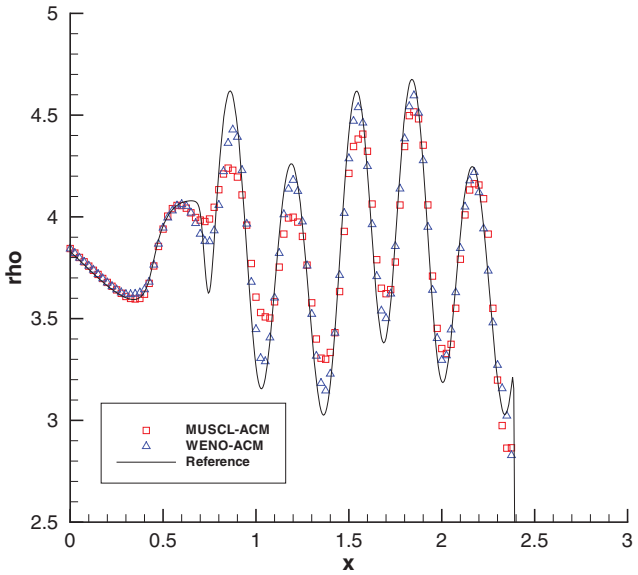

Figure 7. Density distribution at $t = 1.8$ with MUSCL and WENO filters applied globally.

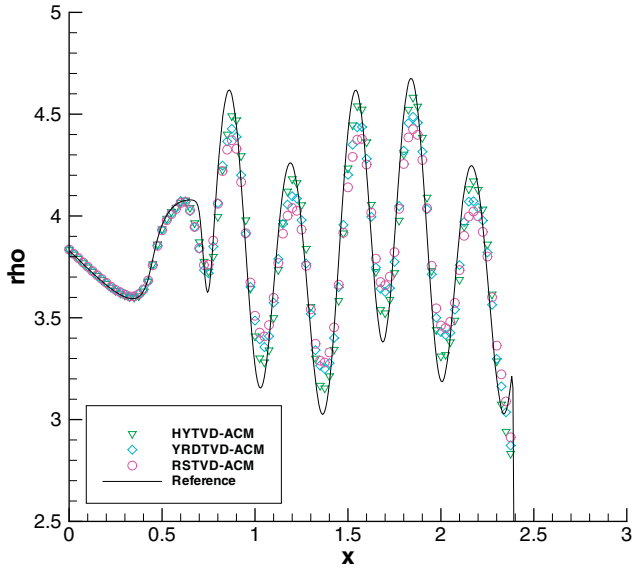

Figure 8. Density distribution at $t = 1.8$ with TVD filters applied locally.

In addition, when the ACM filter is applied in the entire computational domain, it damps out not only the potential oscillations caused by a numerical instability, but also the physical density fluctuations behind the main shock. This situation is more pronounced for the TVD filter as shown in Figures 6 and 8. Adding dissipation to the turbulence fluctuations should be avoided in turbulent

DOI: 10.1002/fld

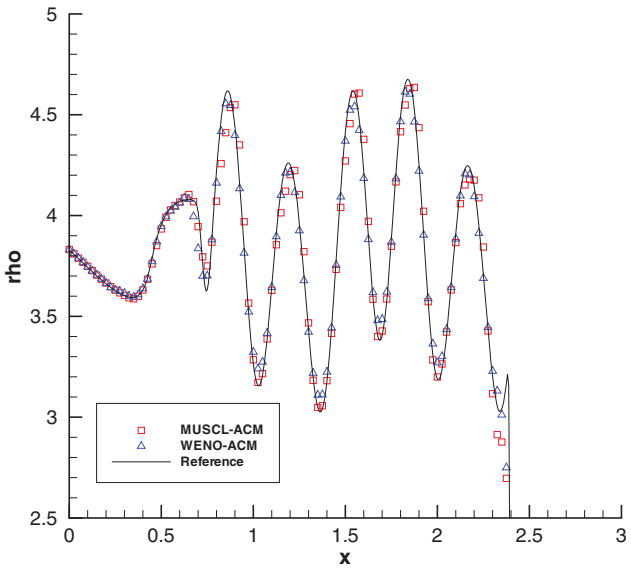

Figure 9. Density distribution at $t = 1.8$ with MUSCL and WENO filters applied locally.

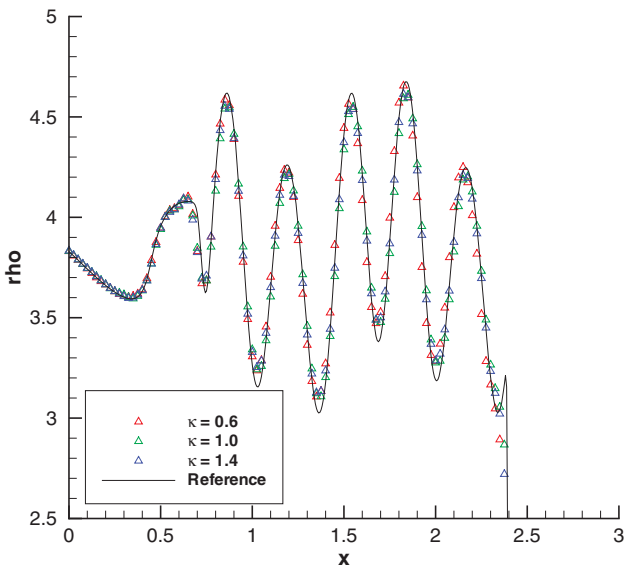

Figure 10. Comparison of different κ on the WENO filter.

flow simulations such as LES or DNS, because it degrades the accuracy of the solutions. For high-order filters such as the WENO filter, the difference between the local and global ACM application is less significant as seen by comparing Figures 7 and 9.

The effects of two parameters, κ and σ, are further investigated. Figure 10 compares the results computed by the local WENO-ACM with three different values, 0.6, 1.0, and 1.4, of the constant

DOI: 10.1002/fld

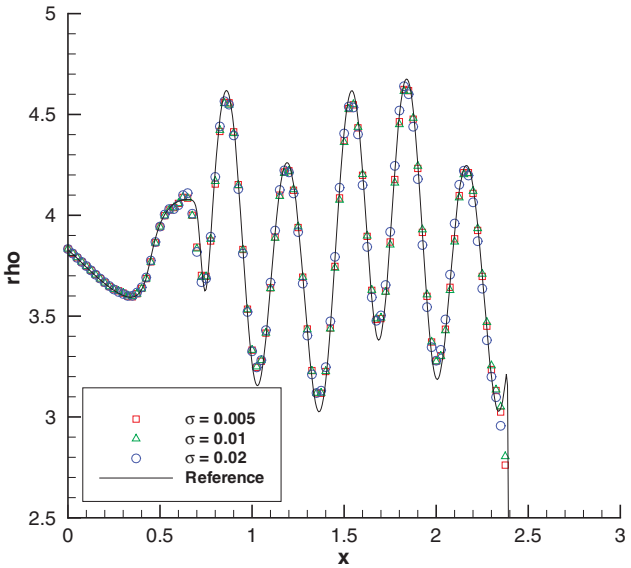

Figure 11. Comparison of different threshold parameters with Equation (24) on WENO filter.

κ, which appears in Equation (16). All results are close to each other and the effect of κ on the WENO filter is insignificant. A value of $\kappa = 1.0$ is used in subsequent cases. The same value of κ is suggested in Reference [12]. For the effect of κ on TVD and MUSCL filters, the reader should refer to Yee *et al.* [8].

Figures 11 and 12 show the effects of three different threshold parameter values of σ (0.005, 0.01, and 0.02) on both shock detectors (Equations (24) and (25)). It should be mentioned that we adopt only the first part (Jameson sensor) of Equation (24), because the curl of the velocity is not applicable in the one-dimensional case. As the plots show, $\sigma = 0.01$ is adequate for both shock detectors, because the variance of the results for the three values of σ is insignificant. Since the effects of different values of σ on the TVD and MUSCL filters are similar to those on the WENO filter, these results are omitted here. It is worth mentioning that if we pick too large a value of σ the code may become unstable because no shock points are filtered. On the other hand, if we choose too small a value of σ, the results would approach the global filtering results. The instantaneous distributions of the two shock detector functions using the WENO filter at $t = 1.8$ are shown in Figures 13 and 14. The threshold values, σ, are also shown by dashed lines. It seems that the main difference between these two shock sensors is the sharpness of the peaks, and $\sigma = 0.01$ picks out not only the main shock but at least two weaker shocks.

3.3. Quasi 1-D inviscid nozzle flow

In contrast to the previous examples which consider a moving shock, this case investigates the shock capturing ability of the ACM filters for a stationary shock within the diverging portion of a nozzle [27]. The nozzle cross-sectional area is described by

$$A(x) = 1.398 + 0.347 \tanh(0.8x - 4) \quad \text{for } 0 < x < 10 \tag{30}$$

DOI: 10.1002/fld

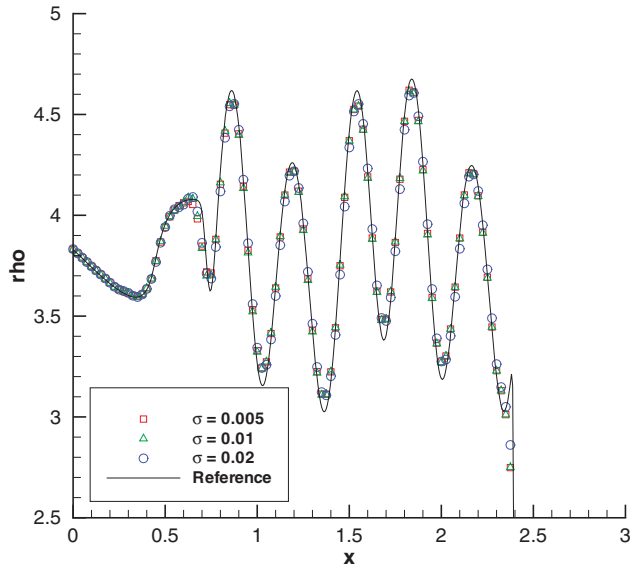

Figure 12. Comparison of different threshold parameters with Equation (25) on WENO filter.

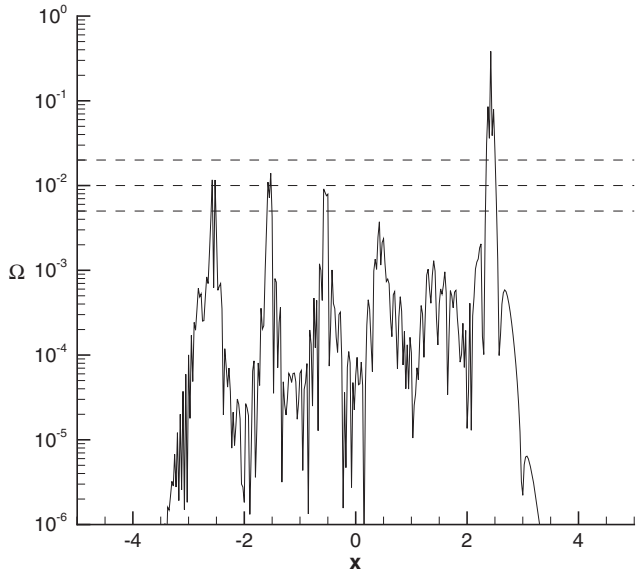

Figure 13. Jameson sensor at $t = 1.8$ computed for the case using WENO-ACM. Dashed lines are the three different values of σ (0.005, 0.01 and 0.02).

Here the distance x is measured in feet. The flow at the nozzle inlet is supersonic and has a Mach number 1.75. The inlet pressure and temperature are 12.5 psi (8.62×10^4 Pa) and 500 R (277.78 K), respectively. At the nozzle exit, the outflow velocity is 566.43 fps (172.65 m/s), which corresponds

DOI: 10.1002/fld

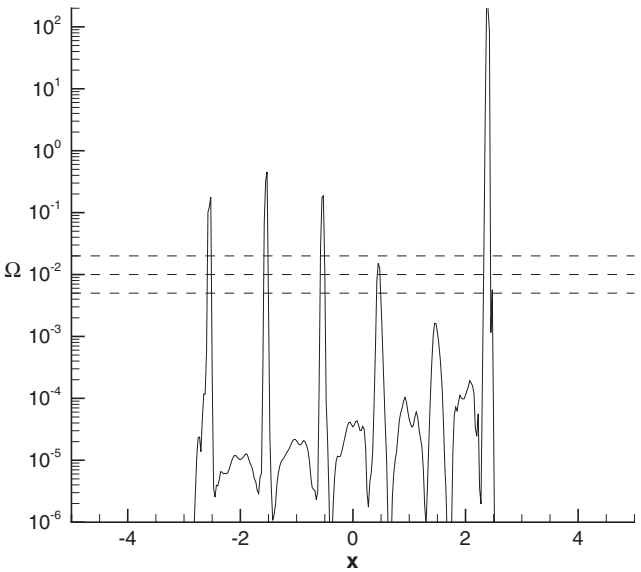

Figure 14. WENO-type sensor at $t = 1.8$ computed for the case using WENO-ACM. Dashed lines are the three different values of σ (0.005, 0.01 and 0.02).

to an exit Mach number 0.414. Under this condition, a normal shock stands at the middle of the nozzle, which has an upstream Mach number 2.1. A uniform mesh with 101 grid points is used in this case, and the initial condition is directly set up from the analytic solution. The analytic solution is computed by the area ratio/Mach number relation.

Figure 15 shows the Mach number distributions computed by three different types of ACM filters. Unlike the moving shock cases, significant oscillations appear near the stationary shock region, especially for the HYTVD and MUSCL filters. However, these numerical oscillations can be damped out as shown in Figure 16, if we apply the ACM filter twice at the end of each full time step. Numerical experiments have shown that as we apply the ACM filter more than twice, the change of the solution becomes insignificant. Therefore, for the sake of saving computational time, applying the ACM filter twice for the stationary normal shock is adequate to damp out the numerical oscillations. It is worth mentioning that for the stationary normal shock this approach works better than performing the ACM filter at each sub-stage of the Runge–Kutta integration.

To test the effect of applying the ACM filter twice for problems not involving a stationary normal shock, the 1-D shock/density oscillation interaction case of Section 3.2 was reconsidered. The results (not shown for brevity) indicate only a minor difference for the WENO filter and a small but noticeable damping with the other filters. For example, relative to filtering once, applying the TVD and MUSCL filters twice causes about 3.5 and 2.4% decreasing of the peak values of density in the region $x \in [0.8, 2.2]$, respectively, while the difference with the WENO filter is less than 0.9%.

3.4. 2-D viscous shock/vortex interactions

This case is used to investigate the ability of the shock-capturing schemes to predict the generation and transport of acoustic waves during a shock vortex interaction [28]. A square domain $2L_0 \times 2L_0$

DOI: 10.1002/fld

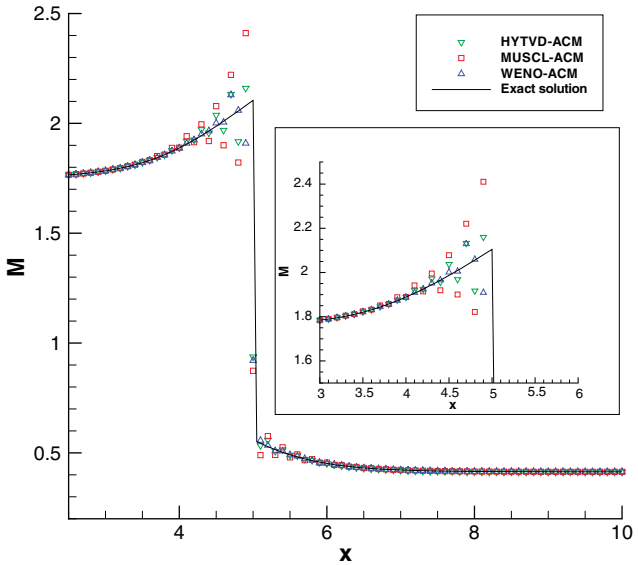

Figure 15. The Mach number distributions of quasi 1D nozzle flow; ACM filter is applied once.

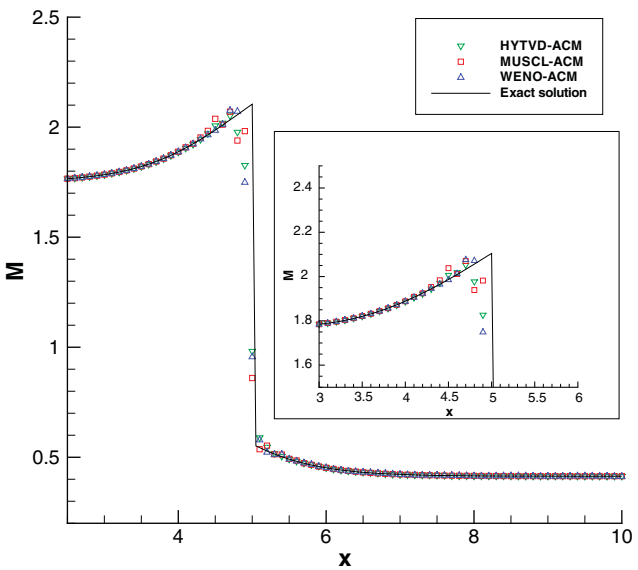

Figure 16. The Mach number distributions of quasi 1D nozzle flow; ACM filter is applied twice.

(where L_0 is the reference length) is considered. The nondimensional computational domain is $[0,2]\times[0,2]$. Two uniform grids with 101×101 and 201×201 points are used, just as in the original reference. The initial condition satisfies the exact Rankine–Hugoniot condition and a

DOI: 10.1002/fld

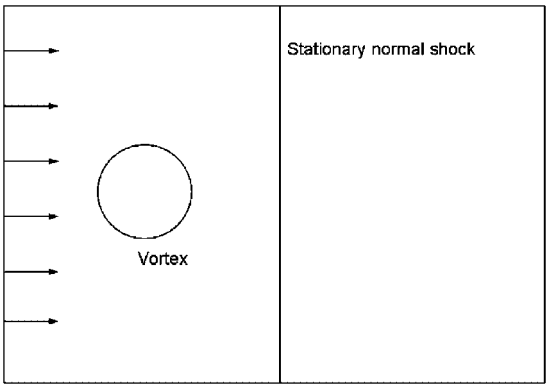

Figure 17. Schematic of the single vortex interacts with a stationary normal shock.

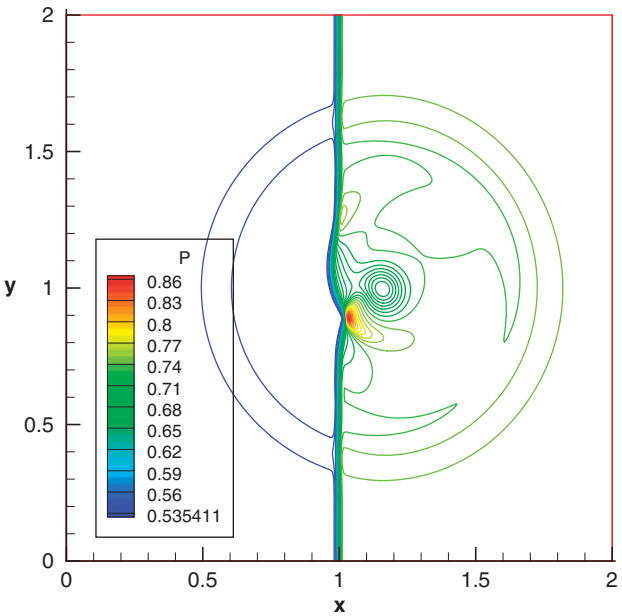

Figure 18. Pressure contour of reference solution at $t=0.7$.

stationary shock is located at $x=1$. An isolated Taylor vortex is added to the uniform flow and is described by the tangential velocity

$$V_\theta = C_1 r e^{-C_2 r^2} \tag{31}$$

with

$$C_1 = \frac{U_c}{r_c} e^{1/2}, \quad C_2 = \frac{1}{2r_c^2}, \quad r = \sqrt{(x-x_0)^2+(y-y_0)^2} \tag{32}$$

DOI: 10.1002/fld

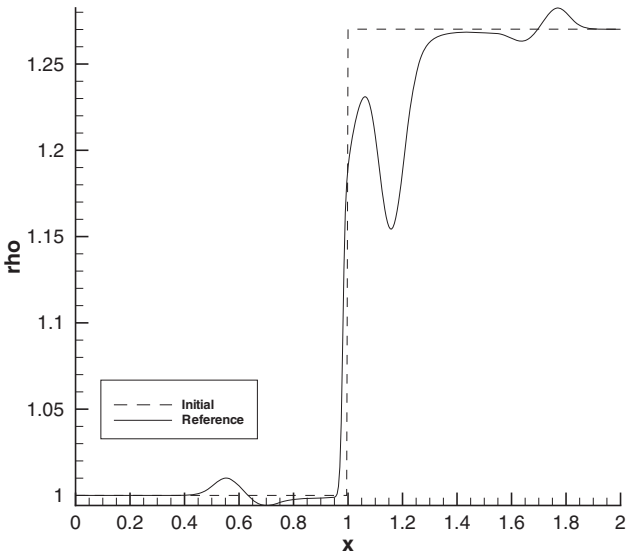

Figure 19. Initial density distribution and final reference solution along $y=1$ at $t=0.7$.

where $r_c=0.075$ and $U_c=0.25$ based on the upstream velocity. The initial position of the vortex center is $(x_0, y_0)=(0.5, 1)$, and the inflow Mach number is 1.1588. A sketch of the initial condition is shown in Figure 17. The Reynolds number based on the uniform upstream velocity and the reference length (L_0) is 2000. A nondimensional time step $\Delta t=4\times 10^{-3}$ is used and the final output time is $t=0.7$. For the local ACM filter cases, the Ducros [24] sensor (Equation (24)) with a threshold parameter $\sigma=0.01$ is used. It should be mentioned that for this low Mach number case applying the ACM filter once per time step is sufficient to damp out the numerical oscillations near the shock. Our numerical experiments have shown that the difference between applying the ACM filter once or twice is quite small.

As the vortex starts to move, it generates a circular acoustic wave which propagates in the radial direction with respect to the vortex center. As time passes, both the acoustic wave and the vortex pass through the stationary shock. Different ACM filter schemes are used to compare the accuracy at both the vortex core and this circular acoustic wave behind the shock. The reference solution is obtained by the local WENO-ACM approach on a fine uniform grid (401×401).

The pressure contour of the reference solution at $t=0.7$ is shown in Figure 18. An acoustic wave is seen spreading outward, as discussed above. Figure 19 shows the density distributions of the reference solution at $t=0.7$ and the initial condition along $y=1$. Along the line of $y=1$, the vortex core at $t=0.7$ is located at $x=1.16$ and a downstream propagating acoustic wave is around $x=1.75$. The density distributions using different types of ACM filters locally and globally on a coarse uniform grid (101×101) along $y=1$ at $t=0.7$ are shown in Figure 20. It can be observed that applying the TVD filter globally cannot resolve the acoustic wave and preserve the strength of the vortex core accurately. The WENO filter demonstrates a superior capability of capturing the acoustic wave and resolving the vortex core compared with the other filters. The results computed using a finer grid (201×201) are shown in Figure 21. With this grid resolution, all the cases (except the global HYTVD-ACM approach) resolve the vortex core and the acoustic wave accurately and become grid independent.

DOI: 10.1002/fld

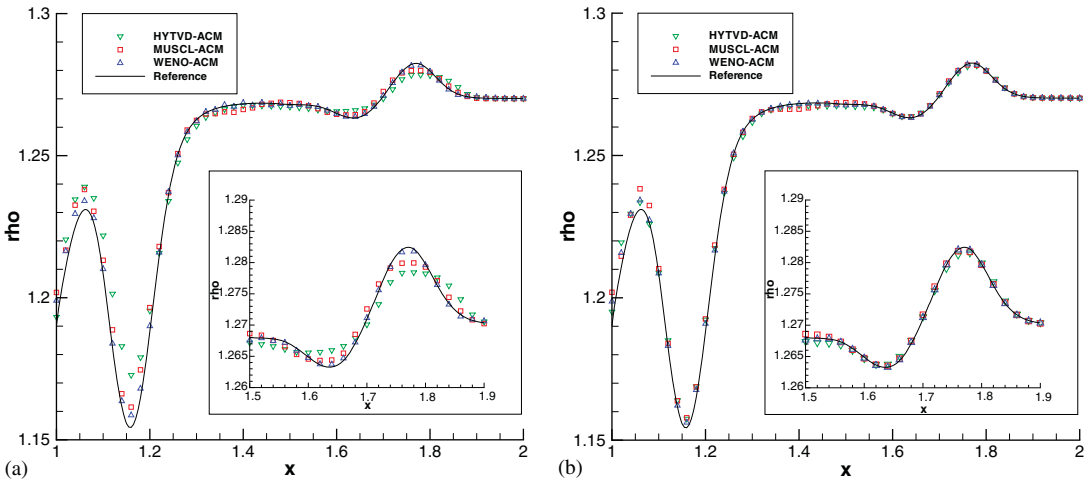

Figure 20. Instantaneous density distributions ((a): global ACM, (b): local ACM) at $t=0.7$ along $y=1$ with a 101×101 grid.

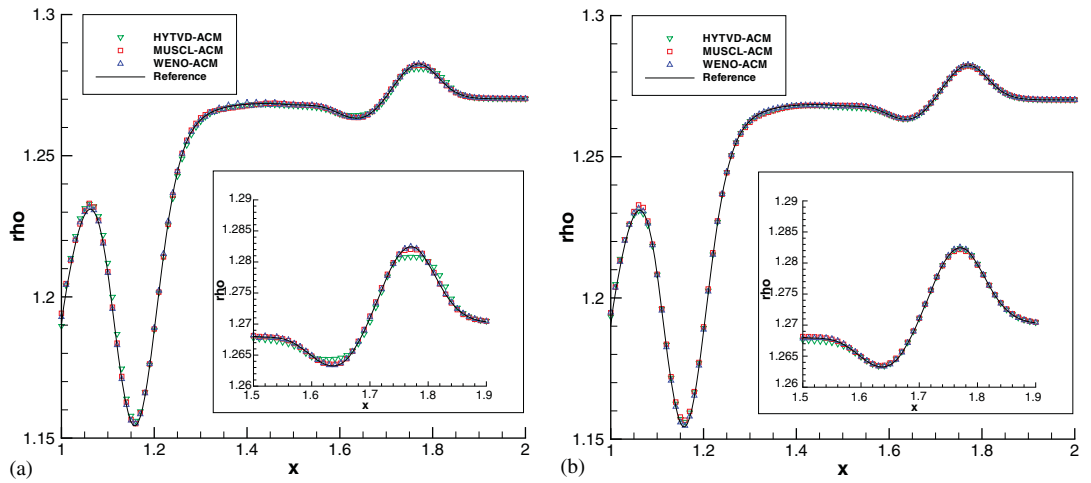

Figure 21. Instantaneous density distributions ((a): global ACM, (b): local ACM) at $t=0.7$ along $y=1$ with a 201×201 grid.

Figure 22 compares the coarse-grid results using three different threshold parameters σ (0.005, 0.01, and 0.02) on the WENO filter. Similar to the 1-D shock/density oscillation case, the effect of σ is insignificant, and all three results overlap with each other.

3.5. Shock/mixing layer interaction

This case is used to test the performance of the shock capturing schemes for interactions of shock waves and shear layers [8]. A spatially developing mixing layer has an initial convective Mach

DOI: 10.1002/fld

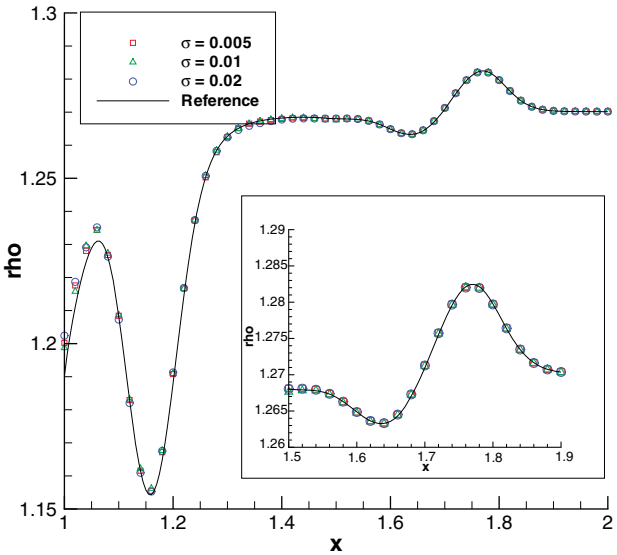

Figure 22. Comparison of different threshold parameters with Ducros sensor on WENO filter.

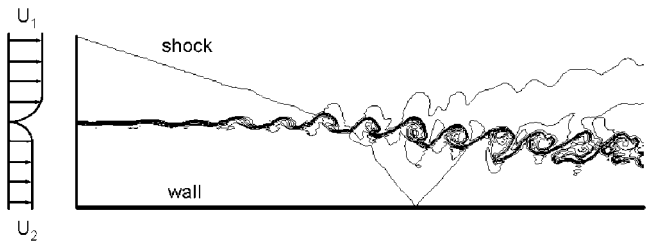

Figure 23. Schematic of the shock impingement on a spatially developing mixing layer.

number of 0.6, and a 12° oblique shock originating from the upper-left corner interacts with the vortices developed from the instability of the shear layer as shown in Figure 23. This oblique shock is deflected by the shear layer and then reflects from the bottom slip wall. At the same time, an expansion fan forms above the shear layer. Downstream, a series of shock waves form around the vortices. The outflow boundary has been arranged to be supersonic everywhere; therefore, a simple first-order extrapolation is used as the outflow boundary condition.

The inflow boundary condition has a hyperbolic tangent velocity profile,

$$u = 2.5 + 0.5 \tanh(2y) \tag{33}$$

and the velocities in the upper and lower streams are $u_1 = 3$ and $u_2 = 2$, respectively. The convective Mach number is

$$M_c = \frac{u_1 - u_2}{c_1 + c_2} = 0.6 \tag{34}$$

DOI: 10.1002/fld

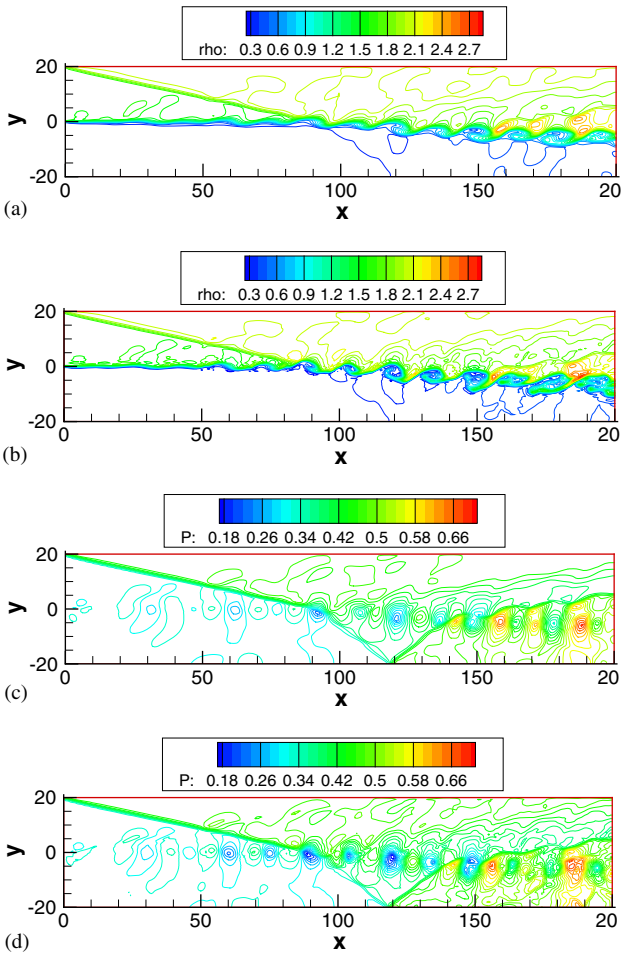

Figure 24. Density ((a) and (b)) and pressure ((c) and (d)) contours using the HYTVD filter: (a) global filtering, $(\max, \min) = (2.577, 0.335)$; (b) local filtering, $(\max, \min) = (2.900, 0.257)$; (c) global filtering, $(\max, \min) = (0.717, 0.258)$; and (d) local filtering, $(\max, \min) = (0.729, 0.170)$.

where c_1 and c_2 are the free stream sound speeds which equal 0.5333 and 1.1333, respectively. These nondimensional velocities and speeds of sound are taken directly from the original reference. The Prandtl number is 0.72 and the Reynolds number based on the velocity jump and vorticity thickness is 500. More detailed boundary information can be found in the same reference. Fluctuations are added to the inflow as

$$v' = \sum_{k=1}^{2} a_k \cos(2\pi k t/\tau + \varphi_k) \exp(-y^2/b) \tag{35}$$

with period $\tau = \lambda/u_c$, wavelength $\lambda = 30$, and convective velocity $u_c = 2.68$. Other constants are $a_1 = 0.05$, $\varphi_1 = 0$, $a_2 = 0.05$, $\varphi_2 = \pi/2$, and $b = 10$. This case was run on a 200×40 domain with a 321×81 grid, which is uniform in the x direction but stretched in the y direction with a minimum

DOI: 10.1002/fld

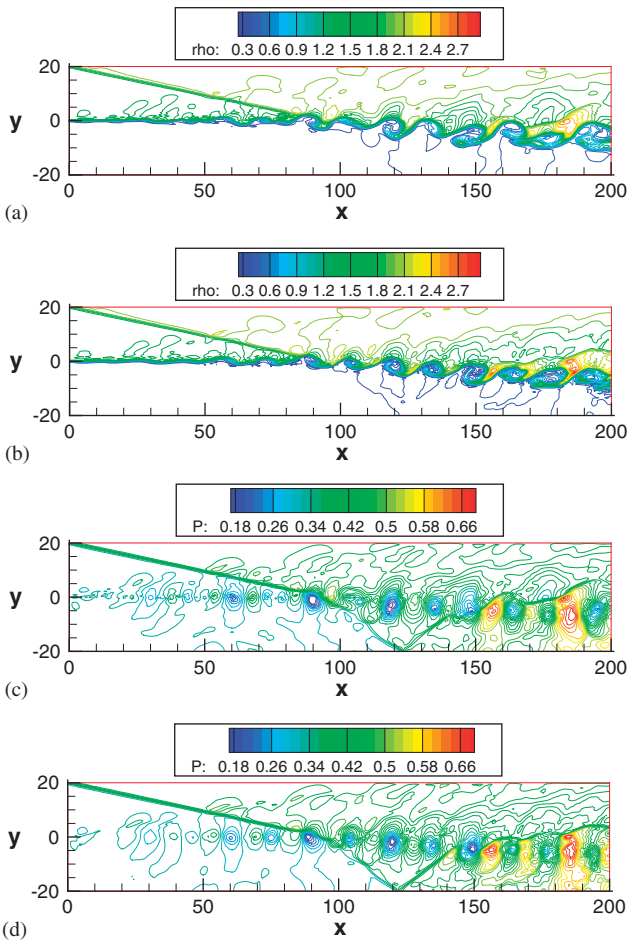

Figure 25. Density ((a) and (b)) and pressure ((c) and (d)) contours using the MUSCL filter: (a) global filtering, $(\max, \min) = (2.703, 0.282)$; (b) local filtering, $(\max, \min) = (2.946, 0.239)$; (c) global filtering, $(\max, \min) = (0.708, 0.146)$; and (d) local filtering, $(\max, \min) = (0.704, 0.156)$.

grid spacing $\Delta y_{\min} = 0.4255$. A constant time step is used with $\Delta t = 0.12$ and the final output time is $t = 120$. The Ducros shock sensor (Equation (24)) with a threshold parameter $\sigma = 0.01$ is used as in the previous case.

As the original reference does not provide quantitative comparison, only qualitative results are presented. Figures 24–26 show the density and pressure contours for each case. From the figures, the solutions with the TVD filter are more diffused. For example, under the same contour levels, the shapes of the vortices are not resolved properly, and the shocklets generated by the vortices in the downstream region are more smeared than the results computed by the other filters. However, both the MUSCL (Figure 25) and WENO (Figure 26) filters provide high quality vortices and downstream shocklet resolution. The effect of the shock detector (i.e. local versus global application of the ACM filter) for the WENO and MUSCL filters is not significant.

DOI: 10.1002/fld

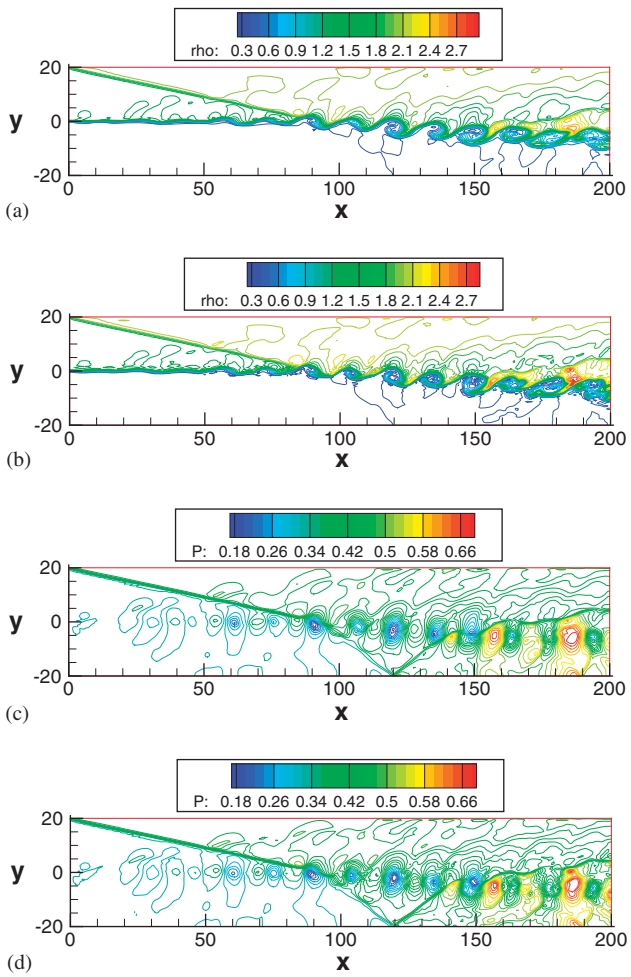

Figure 26. Density ((a) and (b)) and pressure ((c) and (d)) contours using the WENO filter: (a) global filtering, $(\max, \min) = (2.670, 0.296)$; (b) local filtering, $(\max, \min) = (2.843, 0.246)$; (c) global filtering, $(\max, \min) = (0.719, 0.171)$; and (d) local filtering, $(\max, \min) = (0.724, 0.158)$.

The computational time was studied for this case and all the results are compared with a base scheme, which is computed by the compact scheme plus the spatial filter on the same grid. Since the base scheme does not work for cases with shocks, a uniform flow condition is used instead to measure its total computational time. For the global ACM filter approaches, HYTVD, MUSCL, and WENO filters require about 23, 17, and 127% more computational time than the base scheme, respectively. On the other hand, the increase in computational time for the local ACM approaches (compared with the base scheme) is about 56, 50, and 160% for HYTVD, MUSCL, and WENO filters, respectively. It should be mentioned that for the local ACM approach we compute the filter numerical flux everywhere but apply it only in the shock regions as determined by a shock detector. This is the reason that the local ACM approach takes more computational time than the global

DOI: 10.1002/fld

approach. A more efficient method would be to compute the filter numerical flux just in the shock regions.

4. CONCLUSIONS

A Navier–Stokes computational methodology for turbulent supersonic flows based on high-order compact finite difference schemes and characteristic filters has been developed and tested for several test cases. These numerical experiments include a shock tube problem, the interactions of a 1-D moving shock with a sinusoidal density wave, a quasi 1-D nozzle flow, a 2-D stationary shock with a moving vortex, and a 2-D shock/mixing layer interaction. The results show that the high-order characteristic filters, such as the WENO filter, perform better than the low-order filters (such as the TVD and MUSCL filters). Furthermore, the WENO filter is insensitive to the parameters that appear in both the filter schemes and the original shock capturing schemes. In addition, from the previous example of a 1-D shock tube problem, the WENO filter can handle stronger shocks than the other types of ACM filters, but does not dissipate the solution as much as the TVD filter. The reason for this is still an open issue. A possible explanation is that the WENO filter does not rely on any limiter functions like the TVD or MUSCL filters; instead it computes the stencil weights based on the shock location. This may let the WENO filter to add the dissipation in the shock regions more exactly. Numerical experiments have shown that the difference between applying the characteristic filter once or twice per time step is small. For moving shocks, in order to save computational time, applying the filter once is suggested. For some strong stationary normal shock cases, applying the filter twice may be needed to adequately damp out the numerical oscillations. In addition, it is found that applying the WENO filter twice does not cause significant damping in the shock free regions. One disadvantage of the ACM filters for turbulent flows is the difficulty of distinguishing turbulent fluctuations from shocks. This drawback can be remedied by using a shock sensor and then applying the ACM filter locally in the shock regions. At the same time, in order to keep the compact scheme stable, a spatial filter is applied in the shock-free regions. Two shock sensors are considered (one for 1-D problems and another for 2-D problems), and both of them work quite well. In order to trigger the shock sensor, a constant threshold parameter, 0.01, is suggested. This value works well for our 1-D and 2-D test cases. Through several numerical experiments, the results using the local ACM approach show an improvement over global application of the filter, especially for the low-order ACM filters.

ACKNOWLEDGEMENTS

The authors would like to thank Helen Yee for her helpful discussions concerning the formulation and performance of the TVD schemes. The first author gratefully acknowledges the support of the Purdue Research Foundation (PRF)/Computing Research Institute (CRI) Special Incentive Research Grant (SIRG).

REFERENCES

1. Lele SK. Compact finite difference schemes with spectral-like resolution. *Journal of Computational Physics* 1991; **103**(1):16–42.
2. Gaitonde DV, Visbal MR. Further development of a Navier–Stokes solution procedure based on high-order formulas. *AIAA Paper 1999-0557*, 1999.

DOI: 10.1002/fld

3. Visbal MR, Gaitonde DV. High-order-accurate methods for complex unsteady subsonic flows. *AIAA Journal* 1999; **37**(10):1231–1239.
4. Al-Qadi IMA, Scott JN. Simulations of unsteady behavior in under-expanded supersonic rectangular jets. *AIAA Paper 2001-2119*, 2001.
5. Bodony DJ, Lele SK. On using large-eddy simulation for the prediction of noise from cold and heated turbulent jets. *Physics of Fluids* 2005; **17**:085103.
6. Uzun A, Lyrintzis AS, Blaisdell GA. Coupling of integral acoustics methods with LES for jet noise prediction. *International Journal of Aeroacoustics* 2004; **3**(4):297–346.
7. Xie P, Jiang L, Liu C. Weighted compact scheme and smart-filter for 2-D unsteady shock/boundary layer interaction. *AIAA Paper 2006-306*, 2006.
8. Yee HC, Sandham ND, Djomehri MJ. Low-dissipative high-order shock-capturing methods using characteristic-based filters. *Journal of Computational Physics* 1999; **150**:199–238.
9. Garnier E, Mossi M, Sagaut P, Comte P, Deville M. On the use of shock-capturing schemes for large-eddy simulation. *Journal of Computational Physics* 1999; **153**:273–311.
10. Lee S, Lele SK, Moin P. Interaction of isotropic turbulence with shock waves: effect of shock strength. *Journal of Fluid Mechanics* 1997; **340**:225–247.
11. Visbal MR, Gaitonde DV. Shock capturing using compact-differencing-based methods. *AIAA Paper 2005-1265*, 2005.
12. Garnier E, Sagaut P, Deville M. A class of explicit ENO filters with applications to unsteady flows. *Journal of Computational Physics* 2001; **170**(1):184–204.
13. Lo S-C, Blaisdell GA, Lyrintzis AS. High-order shock capturing schemes for turbulence calculations. *AIAA Paper 2007-827*, 2007.
14. Shu CW, Osher S. Efficient implementation of essentially non-oscillatory shock-capturing schemes II. *Journal of Computational Physics* 1989; **83**:32–78.
15. Gaitonde DV, Visbal MR. High-order schemes for Navier–Stokes equations: algorithm and implementation into FDL3DI. *AFRL-VA-WP-TR-1998-3060*, August 1998.
16. Harten A. The artificial compression method for computation of shocks and contact discontinuities: III. Self-adjusting hybrid schemes. *Mathematics of Computation* 1978; **32**(142):363–389.
17. Roe PL. Approximate Riemann solvers, parameter vector, and difference schemes. *Journal of Computational Physics* 1981; **43**:357–372.
18. Yee HC. Upwind and symmetric shock-capturing schemes. *NASA TM-89464*, May 1987.
19. Yee HC, Sjögreen B. Adaptive filtering and limiting in compact high other methods for multiscale gas dynamics and MHD systems. *Computers and Fluids* 2008; **37**:593–619.
20. Garnier E, Sagaut P, Deville M. Large eddy simulation of shock/boundary-layer interaction. *AIAA Journal* 2002; **40**(10):1935–1944.
21. Kim D, Kwon JH. A low dissipative and dispersive scheme with high order weno dissipation for unsteady flow analyses. *AIAA Paper 2004-2705*, 2004.
22. Weirs VG. Low dissipative shock-capturing methods using weighted essentially nonoscillatory and central high resolution filters. *AIAA Paper 2001-2667*, 2001.
23. Shu CW, Osher S. Essentially non-oscillatory and weighted essentially non-oscillatory schemes for hyperbolic conservation laws. *NASA CR-97-206253*, November 1997.
24. Ducros F, Ferrand V, Nicoud F, Weber D, Darracq D, Gacherieu C, Poinsot T. Large-eddy simulation of the shock/turbulence interaction. *Journal of Computational Physics* 1999; **152**:517–549.
25. Jameson A, Schmidt W, Turkel E. Numerical solution of the Euler equations by finite volume methods using Runge Kutta time stepping schemes. *AIAA Paper 1981-1259*, 1981.
26. Sjögreen B, Yee HC. Multiresolution wavelet based adaptive numerical dissipation control for high order methods. *Journal of Scientific Computing* 2004; **20**:211–255.
27. Hoffmann KA, Chiang ST. *Computational Fluid Dynamics* (4th edn), vol. 2. Engineering Education System, Wichita, Kansas, 2000.
28. Tenaud C, Garnier E, Sagaut P. Evaluation of some high-order shock capturing schemes for direct numerical simulation of unsteady two-dimensional free flows. *International Journal for Numerical Methods in Fluids* 2000; **33**:249–278.

DOI: 10.1002/fld